ADVANCING EARTH AND SPACE SCIENCES

Geophysical Research Letters

RESEARCH LETTER
10.1029/2024GL113299

Key Points:

- The strength and pattern of anisotropy in lowermost mantle depends on rheological contrast between thermochemical piles and ambient mantle
- The roots of mantle plumes at the core-mantle boundary display $V_{sv} > V_{sh}$
- $V_{sh} > V_{sv}$ is obtained away from the plume roots and near the subducted slab in the D″ region

Supporting Information:

Supporting Information may be found in the online version of this article.

Correspondence to:

P. Roy,
poulami@gfz.de;
poulami.roy@durham.ac.uk

Citation:

Roy, P., Steinberger, B., Faccenda, M., & Pons, M. (2025). Modeling anisotropic signature of slab-induced mantle plumes from thermochemical piles in the lowermost mantle. *Geophysical Research Letters*, *52*, e2024GL113299. https://doi.org/10.1029/2024GL113299

Received 26 OCT 2024
Accepted 24 APR 2025

Author Contributions:

Conceptualization: Poulami Roy
Investigation: Poulami Roy
Methodology: Poulami Roy, Bernhard Steinberger, Manuele Faccenda, Michaël Pons
Software: Manuele Faccenda
Supervision: Bernhard Steinberger
Visualization: Poulami Roy, Manuele Faccenda
Writing – original draft: Poulami Roy
Writing – review & editing: Bernhard Steinberger, Manuele Faccenda, Michaël Pons

Modeling Anisotropic Signature of Slab-Induced Mantle Plumes From Thermochemical Piles in the Lowermost Mantle

Poulami Roy[1,2], Bernhard Steinberger[1], Manuele Faccenda[3], and Michaël Pons[1]

[1]GFZ Helmholtz Centre for Geosciences, Potsdam, Germany, [2]Durham University, Durham, UK, [3]Dipartimento di Geoscienze, Università degli Studi di Padova, Padova, Italy

Abstract Seismic anisotropy, observed in the lowermost mantle near Large Low-Shear-Velocity Provinces (LLSVPs), is likely caused by strong deformation from mantle flow interacting with these regions and/or plume formation. This study explores slab-induced plume generation from LLSVPs under the assumption that LLSVPs are thermochemical piles and resulting flow behavior using 3-D regional-scale mantle convection models in ASPECT, coupled with mantle fabric simulations in ECOMAN. We tested various models with different LLSVP density and viscosity. The modeling of the crystallographic-preferred orientation with predominant activity of the slip system [001](100) for Bridgmanite and [100](001) for post-Perovskite reveals that substantial seismic anisotropy develops in the lowermost mantle, and specifically (a) at the margins of the rheologically stiffer LLSVP piles where deformation and upwelling of the surrounding mantle take place and fast horizontally polarized shear waves (V_{sh}) transition to fast V_{sv} and (b) within plume roots and conduits where vertically polarized shear waves (V_{sv}) are faster.

Plain Language Summary In the deepest part of the Earth's mantle, seismic wave speeds depend on propagation and/or polarization direction of the wave. This phenomenon, known as seismic anisotropy, has been found to increase toward Large Low-Shear-Velocity Province (LLSVP) edges in multiple regional studies. The anisotropy observed in these regions may result from the deformation of mantle material interacting with the edges of these LLSVPs or the formation of mantle plumes. In this study, we simulate how mantle plumes are generated from these LLSVPs due to the downwelling of cold material and how the mantle flows and deforms in response. Our geodynamic simulations test different scenarios with varying densities and viscosities for the LLSVPs, as well as different deformation mechanisms of lowermost mantle minerals. The results show that the lowermost mantle is mostly isotropic except in regions where plumes rise and slabs subduct. Consistent with seismological observations, we observe vertically polarized shear waves travel faster within plume conduits and horizontally polarized shear waves travel faster near the core-mantle boundary below slabs. At LLSVP boundaries, a transition occurs where mantle upwelling is driven by contrasts in LLSVP and surrounding mantle properties, with faster horizontally polarized shear wave outside and faster vertically polarized shear wave at the margins.

1. Introduction

The D″ region at the base of the mantle is a heterogeneous region which is a host of subducted slab accumulation, continent-sized heterogeneities (i.e., Large Low-Shear-Velocity Provinces or LLSVPs) and is a source of upwelling mantle flow. This region is mainly composed of bridgmanite, post-perovskite, and ferropericlase (Creasy et al., 2020). Seismic observations revealed that structures such as mantle plumes (Stern et al., 2020) and LLSVPs (Ford et al., 2015) in D″ can generate seismic wave velocity dependency on propagation direction and/or polarization (seismic anisotropy) in the lowermost mantle. However, there is no geodynamic study that examines in detail how these processes, specifically plume generation from these piles, affect seismic anisotropy in D″. Our effort here is toward bridging constraints from mineral physics, measurements of seismic anisotropy and models of flow.

The most notable large-scale features in the lower mantle are the two antipodal LLSVPs beneath the Pacific and Atlantic Oceans, which exhibit shear velocity reductions of up to 4% compared to the mantle average (Dziewonski et al., 2010; French & Romanowicz, 2014). While the exact nature of these large features remains a subject of ongoing research (Davaille & Romanowicz, 2020; Davies et al., 2015; Koelemeijer et al., 2017), they are thought to play an important role in Earth's evolution (Burke et al., 2008; Steinberger et al., 2019; Wolf & Evans, 2022). Several studies have revealed that the LLSVPs are distinct structures with different physical properties. Seismic tomography specifically tidal tomography (Lau et al., 2017) and Stoneley modes analysis (Koelemeijer et al., 2017) addressed the density of LLSVP material. LLSVPs are thought to represent piles of either recycled oceanic crust, including mid-ocean ridge basalt (Christensen & Hofmann, 1994; Li & McNamara, 2013; Li et al., 2014; Mulyukova et al., 2015) or iron-rich cumulates (Li, 2015; McNamara & Zhong, 2004, 2005; Nakagawa & Tackley, 2011) that crystallized at a relatively late stage from the basal magma ocean (Labrosse et al., 2007), or rather bundles of plumes (Davaille & Romanowicz, 2020). Deep-seated plumes are typically associated with the margins of the two LLSVPs at the CMB and possibly entrain materials from LLSVPs (Burke et al., 2008) resulting in ocean-island basalts that may have nebular components (Mukhopadhyay, 2012).

The presence of seismic anisotropy acts as a direct indicator of deformation in the Earth's mantle (Long & Becker, 2010; Romanowicz & Wenk, 2017). Lowermost mantle anisotropy has been explained by mechanisms such as slab-driven flow (Asplet et al., 2023; Creasy et al., 2020; Nowacki & Cottaar, 2021; Wolf & Long, 2022) or upwelling flow associated with mantle plumes at the base of the mantle (Ford et al., 2015; Wolf et al., 2019). Furthermore, it has been observed that lowermost mantle anisotropy is often concentrated near the edges of the two LLSVPs (Cottaar & Romanowicz, 2013; Deng et al., 2017; Lynner & Long, 2014; Reiss et al., 2019; Wang & Wen, 2004). This suggests a potential shift in mantle flow direction and/or a localization of the deformation, potentially due to mantle flow interacting with the sides of these provinces (Li & Zhong, 2019; McNamara et al., 2010), or the generation of upwelling of mantle plumes.

In this study, we explore the generation of upwellings from three different scenarios (a) with subducted slab impinging at the CMB, (b) without subduction, and (c) with only slab-induced upwelling but no LLSVPs. We use different viscosity profiles to test the robustness of our model results. Finally, we model shear wave radial anisotropy reflecting the flow behavior in the lower mantle. To better understand Earth's lower mantle, and hence whole-mantle processes, we link recent observations of seismic anisotropy and examine them in their geodynamic context.

2. Methods

We solve the equations for compressible mantle convection using an equation of state that is based on mineral physics data and an Earth-like rheology. Since the focus of this study is deformation in the Earth's mantle, only viscous stresses are considered. This leads to the following equations for conservation of mass, momentum and energy:

$$-\nabla \cdot\ 2\eta\epsilon + \nabla p = \rho g \tag{1}$$

$$\nabla \cdot\ (\rho u) = 0 \tag{2}$$

$$\rho C_p\left(\frac{\partial \mathrm{T}}{\partial \mathrm{t}} + u \cdot \nabla T\right) - \nabla \cdot\ (k\nabla T\ ) = \rho Q + 2\eta\epsilon : \epsilon + \alpha T u \cdot \nabla p \tag{3}$$

where u is the velocity, ϵ is the deviatoric strain rate tensor, p the pressure, and T the temperature field. Additionally, η is the viscosity, ρ is the density, g is the gravity vector, C_p is the specific heat capacity of the material, k is the thermal conductivity, Q is the intrinsic specific heat production, and α is the thermal expansion coefficient.

We set up our mantle convection models using ASPECT (Heister et al., 2017) in a 3D box domain with dimensions of $8{,}700 \times 2{,}900 \times 2{,}900$ km covering the entire mantle depth. We impose a 100 km wide, 300 km deep vertical subduction zone in the box center from the top boundary and place two LLSVP piles (2,000 km wide and 300 km high) on both sides in the D″ (Figure S1 in Supporting Information S1). The strain-induced crystallographic-preferred orientation (CPO) of Lagrangian crystal aggregates is computed using the time-dependent Eulerian flow field from geodynamic models using ECOMAN (Faccenda, 2024). Shear wave radial anisotropy, defined as $\xi = \frac{V_{\mathrm{sh}}^2}{V_{\mathrm{sv}}^2}$, is extracted from the elastic tensor, with positive $\xi - 1 > 0$ indicating faster horizontal shear waves. Detailed setup and methodology are in Texts S1, S2, Figures S3, S8, and Table S3 in Supporting Information S1.

3. Results

Using the time-dependent pressure, temperature, and velocity fields of the geodynamic models, we computed mantle fabrics and associated radial and azimuthal anisotropy. We assume the easy slip system [001](100) of Bridgmanite and [100](001) of post-Perovskite in the computation. The selection of these slip systems is based on the microstructural (Text S3 in Supporting Information S1) and large scale analysis (Text S4 in Supporting Information S1) as a function of Bridgmanite and post-Perovskite CPO. Our strategy here to compute seismic anisotropy is to initially set it to zero throughout the lower mantle, allowing it to develop only when material enters the D″ layer (the bottom 300 km of the mantle). This approach ensures that any observed seismic anisotropy in the lowermost mantle arises solely from processes occurring within this region, consistent with seismological observations of the Earth.

Radial anisotropy was calculated based on the timing of plume surfacing events. After the initial plume pulse, we evaluated radial anisotropy by assessing strain-induced CPO fabrics, computed over the subsequent 20 million years (Myr), and then presented the resulting radial anisotropy (Figure 1, left panels). We also compute radial anisotropy taking into account the plume pulse in the later stage of plume evolution (Figure 1, right panels). The 20 Myr time window is chosen because, after the pulses arrive in the uppermost mantle, it takes approximately 20 Myr for them to spread through the upper mantle and reach a transient steady-state. We also chose a short time window (20 Myr) since the lowermost mantle seismic anisotropy appears to be mainly sensitive to the present day mantle flow field (Ward et al., 2024).

Several model variations have been tested (Figure 1) and their geodynamic descriptions are listed in Tables S1 and S2 in Supporting Information S1. Details of the models in the context of mechanisms of thermochemical plume generation are described in Roy (2024) and Steinberger et al. (2025). In the following, we briefly describe the models. In Figure 1, anisotropy development due to plume generation has been shown together with the boundaries of plumes (shown by black curve), piles (shown by green curve), and slab material (shown by purple curve) along-with the Bridgmanite to post-perovskite phase transition boundary (shown by pink curve), in order to illustrate their relationship. Since our focus is modeling lower mantle anisotropy, we show the radial anisotropy development in the lower mantle (660–2,900 km) with evolution of plumes, piles, and slab for the whole mantle.

- Reference model: The reference model has been constructed with LLSVPs 2% denser (density profile in Figure S2c in Supporting Information S1, red curve) and 10 times more viscous (viscosity profile in Figure S2e in Supporting Information S1, cyan curve) than ambient mantle (density profile in Figure S2c in Supporting Information S1, black curve and viscosity profile in Figure S2e in Supporting Information S1, black curve). The spreading apart of the piles is prevented by the sinking slab, resulting in the plumes remaining located at the pile edges (Figure S4 in Supporting Information S1 left panel). The first plume pulse occurred at 85 Myr for the left plume and 90 Myr for the right plume. Following these initial pulses, the strain-induced CPO fabrics were computed over the subsequent 100–120 Myr, after which we show radial anisotropy (Figure 1, reference model, left panel). Additionally, radial anisotropy was calculated over the subsequent 230–250 Myr after the plumes' second pulse hit at 220 Myr (Figure 1, reference model, right panel). Toward the base of the slab near the CMB, there is enhanced positive anisotropy (earlier stage) which is related to the deformation of post-perovskite at the lowermost mantle. As the slab reaches this region, anisotropy gets widespread around it (later stage). However, inside of the slab is almost isotropic everywhere. LLSVPs exhibit subtle positive anisotropy. Plume roots exhibit negative anisotropy near the CMB and negative anisotropy continues through the plume conduits in the lowermost mantle. Surrounding the plume roots, strong positive anisotropy is observed, spreading more broadly on the slab side and more narrowly on the LLSVP side (later stage). In plume generation zones within the D″ region, the PPv layer thins as it transforms to Brd/Pv at larger depths, consistent with Ward et al. (2024), who also found a thinner PPv layer in upwelling, high-temperature regions, consistent with the positive Clapeyron slope for the Brd to PPv phase transition (Tateno et al., 2009). In the later stages, as more cold slab material accumulates in the lowermost mantle, the thickness of the bottom PPv layer increases where slab impinges the D″ as a result of enhanced Brd to PPv phase transition and the strength of anisotropy has increased just below the impinging slab consistent with Chandler et al. (2021).
- Thermal/no LLSVP: A comparative model was constructed with the same parameters as the reference model but without the presence of LLSVPs. The plumes generated in this model can be classified as slab-triggered, purely thermal plumes (Figure S4 in Supporting Information S1 middle panel). In the earlier stage (115–135 Myr) significant fast V_{sh} anomalies have been developed on both sides of the plume bases

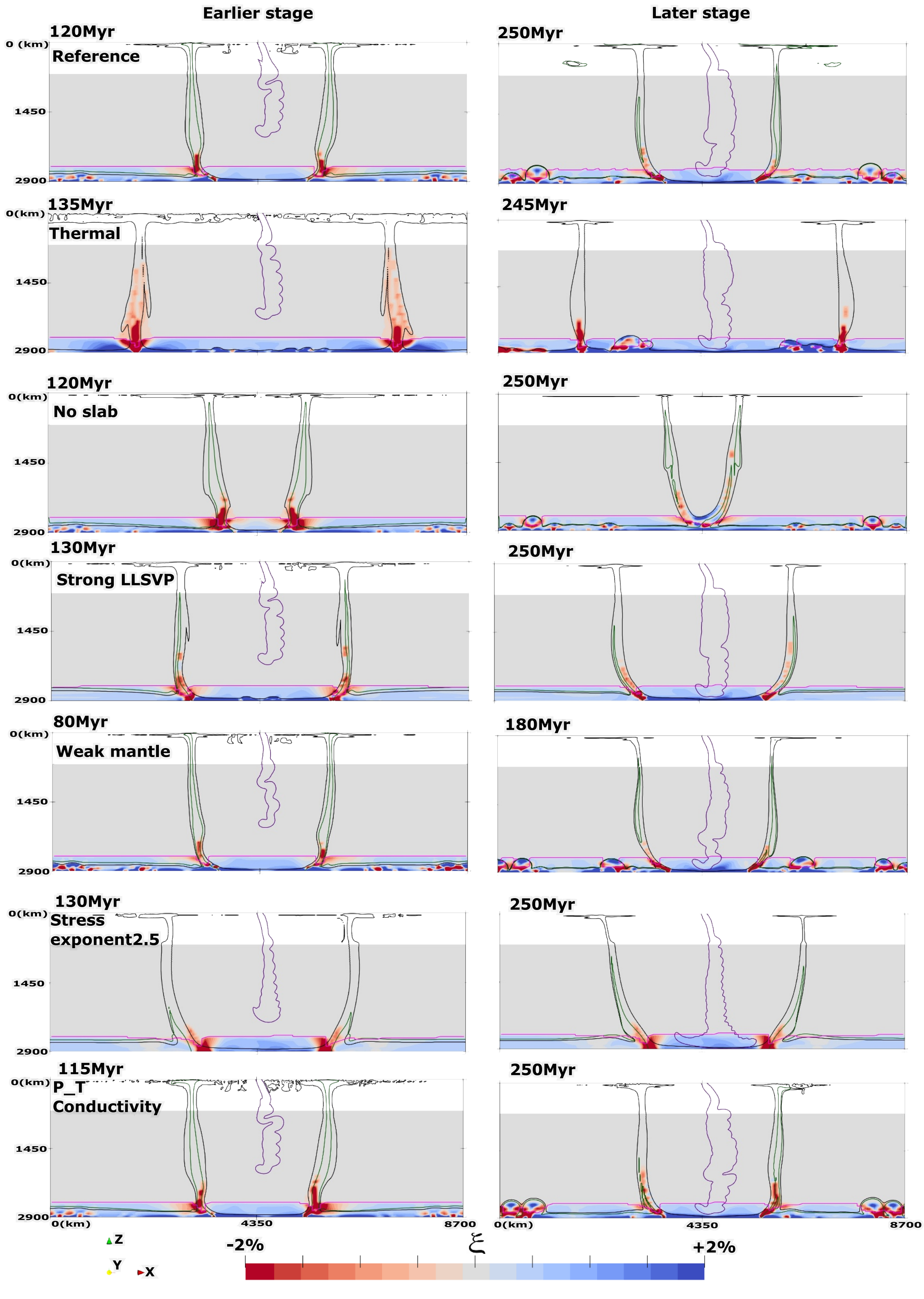

Earlier stage
Later stage
120Myr
Reference
250Myr
135Myr
Thermal
245Myr
120Myr
No slab
250Myr
130Myr
Strong LLSVP
250Myr
80Myr
Weak mantle
180Myr
130Myr
Stress exponent2.5
250Myr
115Myr
P_T Conductivity
250Myr
0 (km)
1450
2900
0(km)
4350
8700
Z
Y
X
-2%
ξ
+2%

Figure 1.

(indicated by dark blue regions), while strong fast V_{sv} anomalies are observed at the plume roots (indicated by dark red regions) in the lowermost mantle (Figure 1, Thermal). The plume conduits show more pronounced vertical anisotropic signature than the reference case. At a later stage (225–245 Myr), the fast V_{sh} anomaly at the base of the slab becomes stronger and the width of the plume conduits becomes narrower leading to narrow fast V_{sv} anomalies inside conduits in the lowermost mantle.

- No slab: The next variation involves the absence of a slab, with the presence of LLSVPs (Figure 1, No slab). This scenario can be considered as thermochemical plumes originating from LLSVPs without any slab influence (Figure S4 in Supporting Information S1 right panel). In this case, the anisotropy developed in the plumes is similar, but the slab-triggered anisotropy in the lower mantle is absent resulting in very shallow positive anisotropy near the CMB in the earlier stage. As the plume roots come close to each other in the later stage due to the spread of piles from opposite sides, fast V_{sv} anomalies replace fast V_{sh} anomalies where PPv transforms to Brd. Mild positive anisotropy is observed away from the plume roots. Inside the LLSVPs are mostly isotropic except for some regions where small scale upwellings produce negative anisotropy at their bases and positive anisotropy at their tops, more prominent in the later stage.
- Strong LLSVP: In the next case the viscosity of the LLSVPs is 100 times greater (Figure S2e in Supporting Information S1, green curve) than that of the ambient mantle (Figure S5 in Supporting Information S1 left panel). In this case earlier and mature stages have been considered as 110–130 and 230–250 Myr, respectively (Figure 1, Strong LLSVP). The anisotropy developed is similar to the reference case, with the exception that weak positive anisotropy developed at the LLSVP edges (earlier stage) but plume roots can still produce strong fast V_{sv} anomalies (earlier and later). A strong LLSVP inhibits any small-scale features to form inside it and becomes almost isotropic to very weakly positively anisotropic.
- Weak mantle: The next case considers that the ambient lower mantle has a viscosity that is half of the reference case (Figure S2d in Supporting Information S1, red curve and Figure S5 in Supporting Information S1 middle panel). While the development of anisotropy is similar to the reference scenario, the shape of the anisotropic regions can vary depending on the plume conduit structure. In this instance, the conduits tend to become more curvilinear (Figure 1, Weak mantle). Since the mantle is weak, plume generation is quick and temporal stages become 60–80 and 160–180 Myr. We observe a clear strong positive anisotropy where the slab touches the CMB at the later stage.
- Stress exponent 2.5: Another variation has weaker depth dependence of viscosity, described by lower mantle stress exponent 2.5 (Figure S2d in Supporting Information S1, blue curve and Figure S5 in Supporting Information S1 right panel). Given the D″ becomes stronger and the lower mantle above it becomes weaker in this case, deformation and hence anisotropy is less focused into the D″ layer. The positive anisotropy at the very base of the slab becomes less strong. Plume roots are significantly negatively anisotropic (Figure 1, Stress exponent 2.5) since strong localized deformation is accumulated at the edges of the more viscous LLSVPs.
- P-T conductivity: The P-T dependent conductivity model produces anisotropy results similar to the reference case. Temporal stages become 95–115 and 230–250 Myr (Figure 1 P-T Conductivity). However, P-T dependent conductivity leads to higher temperature in the lowermost mantle (Figure S2a in Supporting Information S1, blue curve) than in the reference case (Figure S2a in Supporting Information S1, black curve), which causes a massive plume that can reach the surface quicker than the slab sinks to the lower mantle. This allows us to reduce the bottom thermal boundary age from 200 Myr (Figure S6 in Supporting Information S1 right panel) to 100 Myr (Figure S6 in Supporting Information S1 middle panel) leading to results becoming similar again to the reference case.
- Less entrainment: Another model variation involves LLSVP viscosity 10,000 times more (Figure S2e in Supporting Information S1, blue curve) and density 3% higher (Figure S2c in Supporting Information S1, orange curve) than ambient mantle. The very high viscosity and high density of piles make them strong and hard to deform (Figure S6 in Supporting Information S1 left panel). Consequently plume conduits become more vertical and robust. The lateral extent of the region with positive radial anisotropy at the base of the slab

Figure 1. Temporal evolution of shear wave radial anisotropy shown in a 2D slice taken at the middle of the 3D box. From top to bottom panels, results are showing the radial anisotropy development at an earlier (left) and later (right) stage of plume evolution. Plumes are tracked by the 300 K non adiabatic temperature isosurface (black), slabs and Large Low-Shear-Velocity Provinces are identified by a compositional threshold of ≥0.25 and ≥0.45 and colored by purple and green colors, respectively. The bridgmanite to post-perovskite phase transition boundary is shown as pink curve for the post-perovskite compositional threshold 0.5. At each panel, the end time of the 20 Myr period during which radial anisotropy is computed, is given. The crystallographic-preferred orientation evolution and the resulting radial anisotropy development are computed in the bottom 300 km of the mantle only.

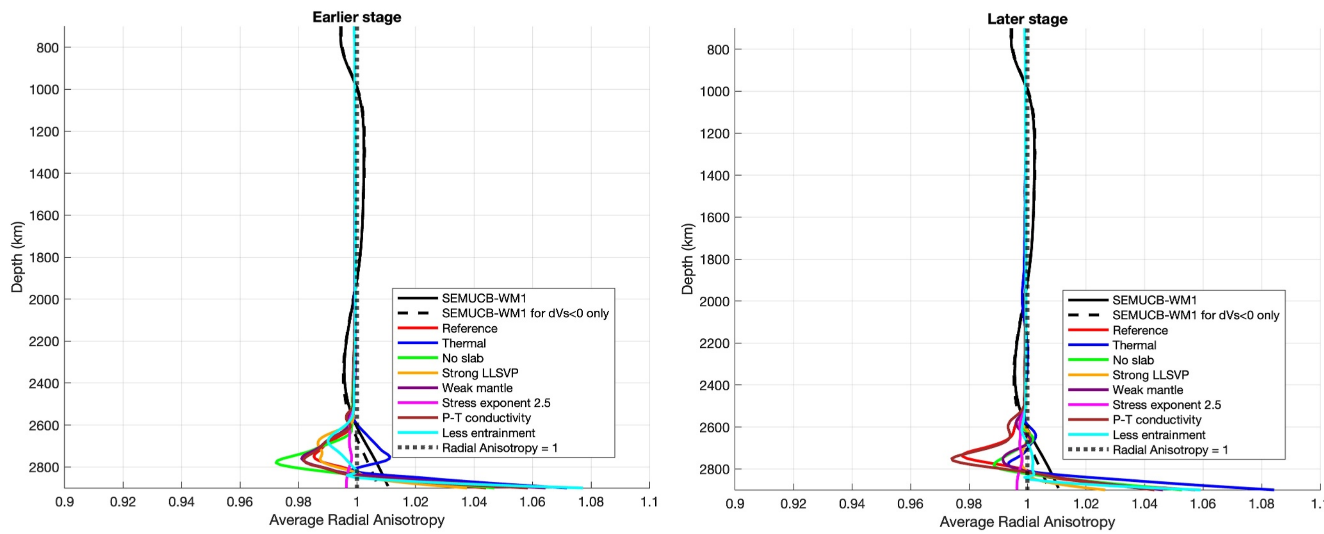

Figure 2. 1D average radial anisotropy of plumes for different model variations, corresponding to the earlier (top figure) and later stages (bottom figure) of the mantle plumes in the lower mantle. The black solid line shows the 1D average radial anisotropy of ambient mantle from the SEMUCB-WM1 tomography model and the black dashed line shows the same restricted to regions where $dV_s < 0$. The black dotted line represents $\xi = 1$.

becomes larger, as the positions of plume roots become more stable since highly viscous LLSVP piles can not spread (Figure S7 in Supporting Information S1, Less entrainment). Temporal stages become 110–130 and 230–250 Myr for earlier and later, respectively.

The average radial anisotropy of the plumes has been plotted in Figure 2 for different model variations. Plumes have been tracked by an isotropic shear wave velocity anomaly (dV_s) threshold of $\leq -1.5\%$ and in this context, we have considered tracking the left plume. For comparison with seismic tomography, the whole mantle tomography model SEMUCBWM1 (French & Romanowicz, 2014) which is shown as black thick lines and also SEMUCBWM1 tomography where dV_s is <0 shown as black dashed lines in Figure 2 are considered. While the former one can be used for ambient mantle anisotropy, the second one can be considered for anisotropy caused by high temperature anomaly. Most of our models show positive anisotropy at the base of the mantle (positive when $\xi - 1 > 0$ and negative when $\xi - 1 < 0$), which changes to negative at around 2,800 km depth. Above 2,600 km, ξ is close to 1 for the rest of the lower mantle. The strength of negative radial anisotropy ranges from 0.97 to 1 (meaning within the range of -3%) and that of positive radial anisotropy is within the range of $+8\%$ for earlier stage and slightly higher than this in the later stage.

Now, if we compare different model variations, we see that the Stress exponent 2.5 model has stronger viscosity (Figure S2d in Supporting Information S1, blue curve) than the reference model (Figure S2d in Supporting Information S1, black curve) in the lowermost mantle. As a result the Stress exponent 2.5 model produces negligible anisotropy at the base of the mantle. In the earlier stage, the No slab model produces the strongest negative anisotropy in the D″. The strongest positive anisotropy is observed in the less entrainment model in the D″. Just above CMB, at the depth of around 2,750 km, only the thermal/No LLSVP model produces positive anisotropy whereas all of the other models show negative anisotropy. In the later stage, the strongest positive anisotropy is developed in the thermal model in D″. The reference model and P-T conductivity model show relatively strong negative anisotropy just above 2,800 km.

Figure 2 shows notable differences between modeled and observed anisotropy in D″. This is expected, as the models represent plumes only, while observations include the broader lowermost mantle (everywhere and regions with $dV_s < 0$). Within plumes, dominant vertical flow leads to a stronger negative extremum. Near the CMB, stronger horizontal flow near plumes (where material flows into them), enhances the positive maximum. As plumes are smaller-scale, the transition from positive to negative anisotropy occurs closer to the boundary. Observed anisotropy is also less positive in regions with $dV_s < 0$, possibly due to plume fabrics. Evaluating D″ anisotropy from global *S*-wave models requires caution due to sensitivity imbalances and trade-offs (Chang et al., 2015; French & Romanowicz, 2014; Kustowski et al., 2008).

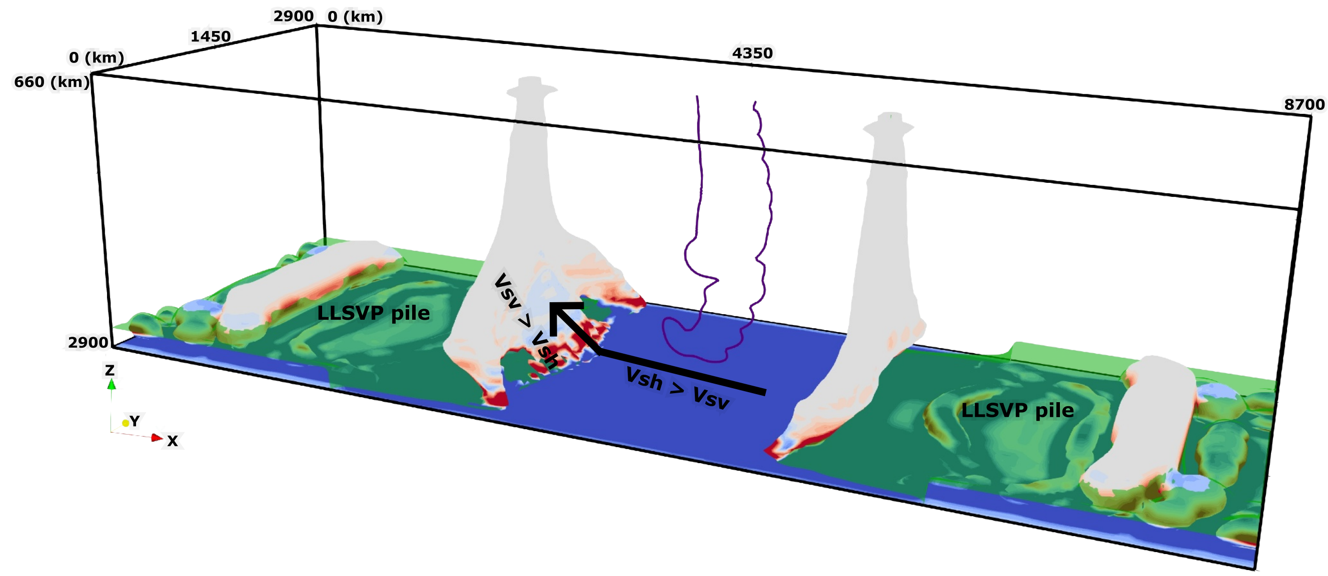

Figure 3. Radial anisotropic signature of 3D thermochemical mantle plumes in the lower mantle. Plumes are tracked by the isosurface of shear wave velocity anomaly $dV_s \le -1.5\%$ and colored by radial anisotropy. The slab (in a 2D slice) and Large Low-Shear-Velocity Provinces are identified by a compositional threshold of $\ge$0.25 and $\ge$0.55 and colored purple and green, respectively. Radial anisotropy scale is the same as in Figure 1. Snapshots are taken after 250 Myr model evolution and radial anisotropy is computed based on the last 20 Myr (230–250 Myr) crystallographic-preferred orientation evolution.

4. Discussion

Our modeled anisotropy reveals that $V_{sv} > V_{sh}$ inside plume conduits and $V_{sh} > V_{sv}$ surrounding plume conduits in the lowermost mantle (Figure 3) which is well aligned with previous seismic observations. Russell et al. (1998) found out there is a transition from horizontal to vertical flow causing ScSV (longitudinal components of motion) waves to travel faster than ScSH (tangential components of motion) waves at the root of the Hawaiian mantle plume at the CMB due to vertically sheared fabric. The ScS splitting measurements done by Wolf et al. (2019), influenced by lowermost mantle anisotropy, demonstrate a shift in the fast splitting direction at the root of the Iceland plume. For two sets of paths sampling outside the low-velocity region, the direction is nearly horizontal (indicating $V_{sh} > V_{sv}$). However, for paths sampling directly beneath Iceland, the direction rotates to nearly vertical (indicating $V_{sv} > V_{sh}$). From our simulation, the strong negative anisotropy of the plume root is associated with the edges of the LLSVP piles most prominently observed in our Strong LLSVP and Less entrainment models, which are well consistent with the seismic anisotropy observation in the lowermost mantle south of Papua New Guinea by Xu et al. (2024). Additionally, the correlation of mantle plumes with LLSVP edges and the resulting $V_{sv} > V_{sh}$ at LLSVP edges from our findings are consistent with multiple seismic observations (Fouch et al., 2001; Ritsema et al., 1998; Vinnik et al., 1995; Wolf & Long, 2023). Strong modeled anisotropy at the plume roots can also be compared with observed stronger seismic anisotropy toward the presumed plume root than away from it (Reiss et al., 2019; Wolf et al., 2024). Comparison with azimuthal anisotropy data further validates our numerical results (Text S5 and Figures S13–S15 in Supporting Information S1).

Creasy et al. (2021) obtained models incorporating post-perovskite (with either a [100](010) or [100](001) dominant slip system) offer the best agreement with the observations in the lowermost mantle beneath Siberia where slab remnants are detected. Chandler et al. (2021) found out post-perovskite (PPv) with either dominant (001) or (010) slip plane can both explain the seismically observed anisotropy in colder regions where downwellings turn to horizontal flow, but only a model with dominant (001) slip plane is matched to seismic observations at the root of hotter large-scale upwellings. Observations of radial anisotropy and splitting in subhorizontal seismic phases are largely consistent with models of postperovskite with (001)-slip (Cottaar et al., 2014). For bridgmanite/perovskite (Brd/Pv), experimental textures are consistent with deformation mechanisms that produce dominant slip on [001](100) (Tsujino et al., 2016). Hence, our selection of the easy slip systems (Figure S11 and S12 in Supporting Information S1) for the most anisotropic phases is supported by the seismic observations and numerical and experimental simulations.

In our geodynamic simulation, we use the reference radial viscosity profile from Steinberger and Calderwood (2006) since we consider this viscosity profile more realistic in terms of fitting with geoid and dynamic topography observations. However, using this viscosity profile does not allow to distinguish between dislocation and diffusion creep. The simulated mantle fabrics and related seismic anisotropy are upper-bound estimates where our model considers deformation in dislocation creep regime. To maintain consistency between the geodynamic and mantle fabric simulations, we limit the anisotropy development to the bottom 300 km of the mantle ensuring the anisotropy has only been developed within the lowermost mantle where deviatoric stresses are relatively high and deformation can be accommodated by dislocation creep processes (Liu et al., 2024; McNamara et al., 2002; Wenk et al., 2006). Simulations where we have relaxed this limitation indicate that the subducted slab can produce positive radial anisotropy on its way down to the lower mantle and negative radial anisotropy inside the plume conduits can continue developing throughout the lower mantle (Text S6 and Figures S16–S18 in Supporting Information S1).

The relation between the sign of radial anisotropy and horizontal versus vertical mantle flow depends on the dominant slip system accommodating deformation (Figures S9 and S10 in Supporting Information S1). According to our results that have been constrained by comparison with seismological observations, positive (negative) radial anisotropy corresponds to horizontal (vertical) flow in the lowermost mantle. This is consistent with previous studies of seismic anisotropy modeling in the lower mantle (e.g., Chang et al., 2016; Ferreira et al., 2019; Mainprice et al., 2008; Sturgeon et al., 2019), and compatible with radial anisotropy associated with the common olivine A-type fabric found in the upper mantle. With the exception of the upper mantle transition zone where wadsleyite fabrics may not follow this general trend (Faccenda, 2014), the correlation between the sign of radial anisotropy and mantle flow direction appears to be homogeneous.

We are also extending our work to global-scale anisotropy modeling within a spherical geometry in an upcoming publication since recent global studies (Li et al., 2024; Peng & Liu, 2022), offer important insights in their ability to match observations.

5. Conclusions

We have tested several properties like temporal evolution of plume surfacing events in the form of earlier versus later stages of plume formation, effect of thermal conductivity, stress exponent, strength of LLSVP, viscosities of ambient mantle, influence of the presence of a slab, morphological differences between thermochemical (presence of LLSVP) and thermal (no LLSVP) plumes and their effects on the anisotropic signature of mantle plumes. After testing rheological and density variations, sensitivity of the anisotropic parameters to different slip systems activities has also been explored. The key findings are the following: For the active slip systems tested, mantle plumes are robust structures in generating fast V_{sv} anomalies in the lowermost mantle. We observe widespread and strong positive radial anisotropy toward the slab side, and narrow positive radially anisotropic regions toward the pile side near the CMB. We find pile-side anisotropy to vary from positive radial anisotropy to isotropy depending on the rheological contrast between piles and ambient mantle. When the subducted slab has reached the lowermost mantle, strong positive radial anisotropy has been generated at the CMB surrounding the slab material. Our findings provide important insights into locating slab positions and upwelling zones, while also helping to constrain the rheological properties of chemical piles in the lowermost mantle.

Acknowledgments
We thank the Computational Infrastructure for Geodynamics (geodynamics.org) which is funded by the National Science Foundation under Award EAR-0949446 and EAR-1550901 for supporting the development of ASPECT. Computations were performed with resources provided by the North-German Supercomputing Alliance (HLRN). PR is funded by The Deutscher Akademischer Austauschdienst (DAAD) for doctoral programme. BS acknowledges funding from the innovation pool of the Helmholtz Association through the Advanced Earth System Modelling Capacity (ESM) activity. MF is supported by the ERC StG 758199 NEWTON. MP is funded by ERC MEET (Grant 856555). We thank Juliane Dannberg, Anne Glerum, Sascha Brune, and Ana Ferreira for helpful discussions. Open Access funding enabled and organized by Projekt DEAL.

Data Availability Statement

The input data and the specific version of codes required to reproduce the models in this study are available from Zenodo (Roy et al., 2024) and are distributed under a Creative Commons Attribution license. The modeling software ASPECT (Heister et al., 2017) was used to compute the geodynamic models and is available under a GPLv2 or newer license. The mantle fabric simulator code ECOMAN (Faccenda, 2024) was used to compute seismic anisotropy and is available under the MIT license.

References

Asplet, J., Wookey, J., & Kendall, M. (2023). Inversion of shear wave waveforms reveal deformation in the lowermost mantle. *Geophysical Journal International*, *232*(1), 97–114. https://doi.org/10.1093/gji/ggac328

Burke, K., Steinberger, B., Torsvik, T. H., & Smethurst, M. A. (2008). Plume generation zones at the margins of large low shear velocity provinces on the core–mantle boundary. *Earth and Planetary Science Letters*, *265*(1–2), 49–60. https://doi.org/10.1016/j.epsl.2007.09.042

Chandler, B. C., Chen, L.-W., Li, M., Romanowicz, B., & Wenk, H.-R. (2021). Seismic anisotropy, dominant slip systems and phase transitions in the lowermost mantle. *Geophysical Journal International*, *227*(3), 1665–1681. https://doi.org/10.1093/gji/ggab278

Chang, S.-J., Ferreira, A. M., & Faccenda, M. (2016). Upper- and mid-mantle interaction between the Samoan plume and the Tonga–Kermadec slabs. *Nature Communications*, *7*(1), 10799. https://doi.org/10.1038/ncomms10799

Chang, S.-J., Ferreira, A. M., Ritsema, J., van Heijst, H. J., & Woodhouse, J. H. (2015). Joint inversion for global isotropic and radially anisotropic mantle structure including crustal thickness perturbations. *Journal of Geophysical Research: Solid Earth*, *120*(6), 4278–4300. https://doi.org/10.1002/2014jb011824

Christensen, U. R., & Hofmann, A. W. (1994). Segregation of subducted oceanic crust in the convecting mantle. *Journal of Geophysical Research*, *99*(B10), 19867–19884. https://doi.org/10.1029/93jb03403

Cottaar, S., Li, M., McNamara, A. K., Romanowicz, B., & Wenk, H.-R. (2014). Synthetic seismic anisotropy models within a slab impinging on the core–mantle boundary. *Geophysical Journal International*, *199*(1), 164–177. https://doi.org/10.1093/gji/ggu244

Cottaar, S., & Romanowicz, B. (2013). Observations of changing anisotropy across the southern margin of the African LLSVP. *Geophysical Journal International*, *195*(2), 1184–1195. https://doi.org/10.1093/gji/ggt285

Creasy, N., Miyagi, L., & Long, M. D. (2020). A library of elastic tensors for lowermost mantle seismic anisotropy studies and comparison with seismic observations. *Geochemistry, Geophysics, Geosystems*, *21*(4), e2019GC008883. https://doi.org/10.1029/2019gc008883

Creasy, N., Pisconti, A., Long, M. D., & Thomas, C. (2021). Modeling of seismic anisotropy observations reveals plausible lowermost mantle flow directions beneath Siberia. *Geochemistry, Geophysics, Geosystems*, *22*(10), e2021GC009924. https://doi.org/10.1029/2021gc009924

Davaille, A., & Romanowicz, B. (2020). Deflating the LLSVPs: Bundles of mantle thermochemical plumes rather than thick stagnant "piles". *Tectonics*, *39*(10), e2020TC006265. https://doi.org/10.1029/2020tc006265

Davies, D., Goes, S., & Sambridge, M. (2015). On the relationship between volcanic hotspot locations, the reconstructed eruption sites of large igneous provinces and deep mantle seismic structure. *Earth and Planetary Science Letters*, *411*, 121–130. https://doi.org/10.1016/j.epsl.2014.11.052

Deng, J., Long, M. D., Creasy, N., Wagner, L., Beck, S., Zandt, G., et al. (2017). Lowermost mantle anisotropy near the eastern edge of the Pacific LLSVP: Constraints from SKS–SKKS splitting intensity measurements. *Geophysical Journal International*, *210*(2), 774–786. https://doi.org/10.1093/gji/ggx190

Dziewonski, A. M., Lekic, V., & Romanowicz, B. A. (2010). Mantle anchor structure: An argument for bottom up tectonics. *Earth and Planetary Science Letters*, *299*(1–2), 69–79. https://doi.org/10.1016/j.epsl.2010.08.013

Faccenda, M. (2014). Mid-mantle anisotropy around subduction zones. *Physics of the Earth and Planetary Interiors*, *227*, 1–19. https://doi.org/10.1016/j.pepi.2013.11.015

Faccenda, M. (2024). mfaccenda/ecoman-geodynamics: Ecoman2.0-geodynamics (2.0) [Dataset]. *Zenodo*. https://doi.org/10.5281/zenodo.10599735

Faccenda, M., VanderBeek, B. P., de Montserrat, A., Yang, J., Rappisi, F., & Ribe, N. (2024). ECOMAN: An open-source package for geodynamic and seismological modelling of mechanical anisotropy. *Solid Earth*, *15*(10), 1241–1264.

Ferreira, A. M., Faccenda, M., Sturgeon, W., Chang, S.-J., & Schardong, L. (2019). Ubiquitous lower-mantle anisotropy beneath subduction zones. *Nature Geoscience*, *12*(4), 301–306. https://doi.org/10.1038/s41561-019-0325-7

Ford, H. A., Long, M. D., He, X., & Lynner, C. (2015). Lowermost mantle flow at the eastern edge of the African large low shear velocity province. *Earth and Planetary Science Letters*, *420*, 12–22. https://doi.org/10.1016/j.epsl.2015.03.029

Fouch, M. J., Fischer, K. M., & Wysession, M. E. (2001). Lowermost mantle anisotropy beneath the Pacific: Imaging the source of the Hawaiian plume. *Earth and Planetary Science Letters*, *190*(3–4), 167–180. https://doi.org/10.1016/s0012-821x(01)00380-6

French, S. W., & Romanowicz, B. A. (2014). Whole-mantle radially anisotropic shear velocity structure from spectral-element waveform tomography. *Geophysical Journal International*, *199*(3), 1303–1327. https://doi.org/10.1093/gji/ggu334

Heister, T., Dannberg, J., Gassmöller, R., & Bangerth, W. (2017). High accuracy mantle convection simulation through modern numerical methods – II: Realistic models and problems. *Geophysical Journal International*, *210*(2), 833–851. https://doi.org/10.1093/gji/ggx195

Koelemeijer, P., Deuss, A., & Ritsema, J. (2017). Density structure of Earth's lowermost mantle from Stoneley mode splitting observations. *Nature Communications*, *8*(1), 15241. https://doi.org/10.1038/ncomms15241

Kustowski, B., Ekström, G., & Dziewonski, A. (2008). Anisotropic shear-wave velocity structure of the Earth's mantle: A global model. *Journal of Geophysical Research*, *113*(B6), 303–318. https://doi.org/10.1029/2007jb005169

Labrosse, S., Hernlund, J., & Coltice, N. (2007). A crystallizing dense magma ocean at the base of the Earth's mantle. *Nature*, *450*(7171), 866–869. https://doi.org/10.1038/nature06355

Lau, H. C., Mitrovica, J. X., Davis, J. L., Tromp, J., Yang, H.-Y., & Al-Attar, D. (2017). Tidal tomography constrains Earth's deep-mantle buoyancy. *Nature*, *551*(7680), 321–326. https://doi.org/10.1038/nature24452

Li, M. (2015). *Thermochemical structure and dynamics of Earth's lowermost mantle*. Arizona State University. https://keep.lib.asu.edu/items/153329

Li, M., & McNamara, A. K. (2013). The difficulty for subducted oceanic crust to accumulate at the Earth's core-mantle boundary. *Journal of Geophysical Research: Solid Earth*, *118*(4), 1807–1816. https://doi.org/10.1002/jgrb.50156

Li, M., McNamara, A. K., & Garnero, E. J. (2014). Chemical complexity of hotspots caused by cycling oceanic crust through mantle reservoirs. *Nature Geoscience*, *7*(5), 366–370. https://doi.org/10.1038/ngeo2120

Li, M., Wolf, J., Garnero, E., & Long, M. D. (2024). Flow and deformation in Earth's deepest mantle: Insights from geodynamic modeling and comparisons with seismic observations. *Journal of Geophysical Research: Solid Earth*, *129*(12), e2024JB029058. https://doi.org/10.1029/2024jb029058

Li, M., & Zhong, S. (2019). Lateral motion of mantle plumes in 3-D geodynamic models. *Geophysical Research Letters*, *46*(9), 4685–4693. https://doi.org/10.1029/2018gl081404

Liu, Y., Yang, T., Wang, K., Wang, X., & Li, Y. (2024). Influence of grain size evolution on mantle plume and LLSVP dynamics. *Geochemistry, Geophysics, Geosystems*, *25*(11), e2024GC011807. https://doi.org/10.1029/2024gc011807

Long, M. D., & Becker, T. W. (2010). Mantle dynamics and seismic anisotropy. *Earth and Planetary Science Letters*, *297*(3–4), 341–354. https://doi.org/10.1016/j.epsl.2010.06.036

Lynner, C., & Long, M. D. (2014). Lowermost mantle anisotropy and deformation along the boundary of the African LLSVP. *Geophysical Research Letters*, *41*(10), 3447–3454. https://doi.org/10.1002/2014gl059875

Mainprice, D., Tommasi, A., Ferr´e, D., Carrez, P., & Cordier, P. (2008). Predicted glide systems and crystal preferred orientations of polycrystalline silicate Mg-Perovskite at high pressure: Implications for the seismic anisotropy in the lower mantle. *Earth and Planetary Science Letters*, *271*(1–4), 135–144. https://doi.org/10.1016/j.epsl.2008.03.058

McNamara, A. K., Garnero, E. J., & Rost, S. (2010). Tracking deep mantle reservoirs with ultra-low velocity zones. *Earth and Planetary Science Letters*, *299*(1–2), 1–9. https://doi.org/10.1016/j.epsl.2010.07.042

McNamara, A. K., Van Keken, P. E., & Karato, S.-I. (2002). Development of anisotropic structure in the Earth's lower mantle by solid-state convection. *Nature*, *416*(6878), 310–314. https://doi.org/10.1038/416310a

McNamara, A. K., & Zhong, S. (2004). Thermochemical structures within a spherical mantle: Superplumes or piles? *Journal of Geophysical Research*, *109*(B7), B07402. https://doi.org/10.1029/2003jb002847

McNamara, A. K., & Zhong, S. (2005). Thermochemical structures beneath Africa and the Pacific Ocean. *Nature*, *437*(7062), 1136–1139. https://doi.org/10.1038/nature04066

Mukhopadhyay, S. (2012). Early differentiation and volatile accretion recorded in deep mantle neon and xenon. *Nature*, *486*(7401), 101–104. https://doi.org/10.1038/nature11141

Mulyukova, E., Steinberger, B., Dabrowski, M., & Sobolev, S. V. (2015). Survival of LLSVPs for billions of years in a vigorously convecting mantle: Replenishment and destruction of chemical anomaly. *Journal of Geophysical Research: Solid Earth*, *120*(5), 3824–3847. https://doi.org/10.1002/2014jb011688

Nakagawa, T., & Tackley, P. J. (2011). Effects of low-viscosity post-perovskite on thermochemical mantle convection in a 3-D spherical shell. *Geophysical Research Letters*, *38*(4), L04309. https://doi.org/10.1029/2010gl046494

Nowacki, A., & Cottaar, S. (2021). Toward imaging flow at the base of the mantle with seismic, mineral physics, and geodynamic constraints. In *Mantle convection and surface expressions* (pp. 329–352).

Peng, D., & Liu, L. (2022). Quantifying slab sinking rates using global geodynamic models with data-assimilation. *Earth-Science Reviews*, *230*, 104039. https://doi.org/10.1016/j.earscirev.2022.104039

Reiss, M. C., Long, M. D., & Creasy, N. (2019). Lowermost mantle anisotropy beneath Africa from differential SKS-SKKS shear-wave splitting. *Journal of Geophysical Research: Solid Earth*, *124*(8), 8540–8564. https://doi.org/10.1029/2018jb017160

Ritsema, J., Lay, T., Garnero, E. J., & Benz, H. (1998). Seismic anisotropy in the lowermost mantle beneath the Pacific. *Geophysical Research Letters*, *25*(8), 1229–1232. https://doi.org/10.1029/98gl00913

Romanowicz, B., & Wenk, H.-R. (2017). Anisotropy in the deep Earth. *Physics of the Earth and Planetary Interiors*, *269*, 58–90. https://doi.org/10.1016/j.pepi.2017.05.005

Roy, P. (2024). *Lower mantle anisotropy due to plume generation from large low-shear velocity provinces*. (PhD dissertation). Universität Potsdam. Retrieved from https://publishup.uni-potsdam.de/frontdoor/index/index/docId/66761

Roy, P., Steinberger, B., Faccenda, M., & Pons, M. (2024). Modeling anisotropic signature of slab-induced mantle plumes from thermochemical piles in the lower mantle [Dataset]. *Zenodo*. https://doi.org/10.5281/zenodo.13983974; https://github.com/poulamiiroy/Preprocess_ECOMAN

Russell, S. A., Lay, T., & Garnero, E. J. (1998). Seismic evidence for small-scale dynamics in the lowermost mantle at the root of the Hawaiian hotspot. *Nature*, *396*(6708), 255–258. https://doi.org/10.1038/24364

Steinberger, B., & Calderwood, A. R. (2006). Models of large-scale viscous flow in the Earth's mantle with constraints from mineral physics and surface observations. *Geophysical Journal International*, *167*(3), 1461–1481. https://doi.org/10.1111/j.1365-246x.2006.03131.x

Steinberger, B., Nelson, P. L., Grand, S. P., & Wang, W. (2019). Yellowstone plume conduit tilt caused by large-scale mantle flow. *Geochemistry, Geophysics, Geosystems*, *20*(12), 5896–5912. https://doi.org/10.1029/2019gc008490

Steinberger, B., Roy, P., Pons-Rallo, M. V., & Jopke, M. P. (2025). Why are plume excess temperatures much less than the temperature drop across the lowermost mantle thermal boundary layer? *Journal of Geophysical Research: Solid Earth*, *130*(4), e2024JB030111. https://doi.org/10.1029/2024jb030111

Stern, T., Lamb, S., Moore, J. D. P., Okaya, D., & Hochmuth, K. (2020). High mantle seismic P-wave speeds as a signature for gravitational spreading of superplumes. *Science Advances*, *6*(22), eaba7118. https://doi.org/10.1126/sciadv.aba7118

Sturgeon, W., Ferreira, A. M., Faccenda, M., Chang, S.-J., & Schardong, L. (2019). On the origin of radial anisotropy near subducted slabs in the midmantle. *Geochemistry, Geophysics, Geosystems*, *20*(11), 5105–5125. https://doi.org/10.1029/2019gc008462

Tateno, S., Hirose, K., Sata, N., & Ohishi, Y. (2009). Determination of post-perovskite phase transition boundary up to 4400 K and implications for thermal structure in D″ layer. *Earth and Planetary Science Letters*, *277*(1–2), 130–136. https://doi.org/10.1016/j.epsl.2008.10.004

Tsujino, N., Nishihara, Y., Yamazaki, D., Seto, Y., Higo, Y., & Takahashi, E. (2016). Mantle dynamics inferred from the crystallographic preferred orientation of bridgmanite. *Nature*, *539*(7627), 81–84. https://doi.org/10.1038/nature19777

Vinnik, L., Romanowicz, B., Le Stunff, Y., & Makeyeva, L. (1995). Seismic anisotropy in the D″ layer. *Geophysical Research Letters*, *22*(13), 1657–1660. https://doi.org/10.1029/95gl01327

Wang, Y., & Wen, L. (2004). Mapping the geometry and geographic distribution of a very low velocity province at the base of the Earth's mantle. *Journal of Geophysical Research*, *109*(B10), B10305. https://doi.org/10.1029/2003jb002674

Ward, J., Walker, A. M., Nowacki, A., Panton, J., & Davies, H. (2024). The sensitivity of lowermost mantle anisotropy to past mantle convection. *Physics of the Earth and Planetary Interiors*, *356*, 107264. https://doi.org/10.1016/j.pepi.2024.107264

Wenk, H.-R., Speziale, S., McNamara, A. K., & Garnero, E. (2006). Modeling lower mantle anisotropy development in a subducting slab. *Earth and Planetary Science Letters*, *245*(1–2), 302–314. https://doi.org/10.1016/j.epsl.2006.02.028

Wolf, J., Creasy, N., Pisconti, A., Long, M. D., & Thomas, C. (2019). An investigation of seismic anisotropy in the lowermost mantle beneath Iceland. *Geophysical Journal International*, *219*(Supplement 1), S152–S166. https://doi.org/10.1093/gji/ggz312

Wolf, J., & Evans, D. A. D. (2022). Reconciling supercontinent cycle models with ancient subduction zones. *Earth and Planetary Science Letters*, *578*, 117293. https://doi.org/10.1016/j.epsl.2021.117293

Wolf, J., Li, M., Haws, A. A., & Long, M. D. (2024). Strong seismic anisotropy due to upwelling flow at the root of the Yellowstone mantle plume. *Geology*, *52*(5), 379–382. https://doi.org/10.1130/g51919.1

Wolf, J., & Long, M. D. (2022). Slab-driven flow at the base of the mantle beneath the northeastern Pacific Ocean. *Earth and Planetary Science Letters*, *594*, 117758. https://doi.org/10.1016/j.epsl.2022.117758

Wolf, J., & Long, M. D. (2023). Lowermost mantle structure beneath the central Pacific Ocean: Ultralow velocity zones and seismic anisotropy. *Geochemistry, Geophysics, Geosystems*, *24*(6), e2022GC010853. https://doi.org/10.1029/2022gc010853

Xu, E., Wolf, J., Frost, D., Li, M., & Long, M. D. (2024). *Deep mantle deformation near Australia linked to large low velocity province and mantle upwelling*. Authorea Preprints.

References From the Supporting Information

Bangerth, W., Dannberg, J., Fraters, M., Gassmoeller, R., Glerum, A., Heister, T., et al. (2024). ASPECT: Advanced solver for planetary evolution, convection, and tectonics, user manual. https://doi.org/10.6084/m9.figshare.4865333

Christensen, U. (1983). Convection in a variable-viscosity fluid: Newtonian versus powerlaw rheology. *Earth and Planetary Science Letters*, *64*(1), 153–162. https://doi.org/10.1016/0012-821x(83)90060-2

Connolly, J. (2009). The geodynamic equation of state: What and how. *Geochemistry, Geophysics, Geosystems*, *10*(10), Q10014. https://doi.org/10.1029/2009gc002540

Dziewonski, A. M., & Anderson, D. L. (1981). Preliminary reference Earth model. *Physics of the Earth and Planetary Interiors*, *25*(4), 297–356. https://doi.org/10.1016/0031-9201(81)90046-7

Faccenda, M. (2024). Ecoman2.0-geodynamics. *Zenodo*. https://doi.org/10.5281/zenodo.10599735

Faccenda, M., & Capitanio, F. A. (2012). Seismic anisotropy around subduction zones: Insights from three-dimensional modeling of upper mantle deformation and SKS splitting. *Geophysical Journal International*, *190*(1), 1–11.

Faccenda, M., & Capitanio, F. A. (2013). Development of mantle seismic anisotropy during subduction-induced 3-D flow. *Geophysical Research Letters*, *40*(16), 3466–3470. https://doi.org/10.1029/2012GL051988

Gale, A., Dalton, C. A., Langmuir, C. H., Su, Y., & Schilling, J.-G. (2013). The mean composition of ocean ridge basalts. *Geochemistry, Geophysics, Geosystems*, *14*(3), 489–518. https://doi.org/10.1002/ggge.20038

Kaminski, E., Ribe, N. M., & Browaeys, J. T. (2004). D-rex, a program for calculation of seismic anisotropy due to crystal lattice preferred orientation in the convective upper mantle. *Geophysical Journal International*, *158*(2), 744–752. https://doi.org/10.1111/j.1365-246x.2004.02308.x

Kronbichler, M., Heister, T., & Bangerth, W. (2012). High accuracy mantle convection simulation through modern numerical methods. *Geophysical Journal International*, *191*(1), 12–29. https://doi.org/10.1111/j.1365-246x.2012.05609.x

Lutz, K. A., Long, M. D., Creasy, N., & Deng, J. (2020). Seismic anisotropy in the lowermost mantle beneath North America from SKS-SKKS splitting intensity discrepancies. *Physics of the Earth and Planetary Interiors*, *305*, 106504. https://doi.org/10.1016/j.pepi.2020.106504

Mainprice, D., Hielscher, R., & Schaeben, H. (2011). Calculating anisotropic physical properties from texture data using the MTEX open-source package. *Geological Society, London, Special Publications*, *360*(1), 175–192. https://doi.org/10.1144/sp360.10

Marquardt, H., Speziale, S., Reichmann, H. J., Frost, D. J., Schilling, F. R., & Garnero, E. J. (2009). Elastic shear anisotropy of ferropericlase in Earth's lower mantle. *Science*, *324*(5924), 224–226. https://doi.org/10.1126/science.1169365

Maupin, V., Garnero, E. J., Lay, T., & Fouch, M. J. (2005). Azimuthal anisotropy in the D″ layer beneath the Caribbean. *Journal of Geophysical Research*, *110*(B8), B08301. https://doi.org/10.1029/2004jb003506

Nakagawa, T., Jackson, M. G., Van Keken, P. E., Kuritani, T., Tatsumi, Y., & Miyajima, N. (2010). Deep mantle structure as revealed by Pb isotopes in volcanic rocks. *Science*, *327*(5966), 193–195.

Oganov, A. R., & Ono, S. (2004). Theoretical and experimental evidence for a postperovskite phase of $MgSiO_3$ in Earth's D″ layer. *Nature*, *430*(6998), 445–448. https://doi.org/10.1038/nature02701

Ringwood, A., & Irifune, T. (1988). Nature of the 650–km seismic discontinuity: Implications for mantle dynamics and differentiation. *Nature*, *331*(6152), 131–136. https://doi.org/10.1038/331131a0

Stackhouse, S., Stixrude, L., & Karki, B. B. (2015). First-principles calculations of the lattice thermal conductivity of the lower mantle. *Earth and Planetary Science Letters*, *427*, 11–17. https://doi.org/10.1016/j.epsl.2015.06.050

Stixrude, L., & Lithgow-Bertelloni, C. (2011). Thermodynamics of mantle minerals-II. Phase equilibria. *Geophysical Journal International*, *184*(3), 1180–1213. https://doi.org/10.1111/j.1365-246x.2010.04890.x

Tommasi, A., Mainprice, D., Cordier, P., Thoraval, C., & Couvy, H. (2004). Strain-induced seismic anisotropy of wadsleyite polycrystals and flow patterns in the mantle transition zone. *Journal of Geophysical Research*, *109*(B12), B12405. https://doi.org/10.1029/2004jb003158

Tosi, N., Yuen, D. A., de Koker, N., & Wentzcovitch, R. M. (2013). Mantle dynamics with pressure-and temperature-dependent thermal expansivity and conductivity. *Physics of the Earth and Planetary Interiors*, *217*, 48–58. https://doi.org/10.1016/j.pepi.2013.02.004

Wentzcovitch, R., Karki, B., Cococcioni, M., & de Gironcoli, S. (2004). Properties of $MgSiO_3$-perovskite: Insights on the nature of the Earth's lower mantle. *Physical Review Letters*, *92*.

Zhang, S., Cottaar, S., Liu, T., Stackhouse, S., & Militzer, B. (2016). High-pressure, temperature elasticity of Fe-and Al-bearing $MgSiO_3$: Implications for the Earth's lower mantle. *Earth and Planetary Science Letters*, *434*, 264–273. https://doi.org/10.1016/j.epsl.2015.11.030

Zhang, Z., Stixrude, L., & Brodholt, J. (2013). Elastic properties of $MgSiO_3$-perovskite under lower mantle conditions and the composition of the deep Earth. *Earth and Planetary Science Letters*, *379*, 1–12. https://doi.org/10.1016/j.epsl.2013.07.034